

SUPERMASSIVE BLACK HOLES WITH HIGH ACCRETION RATES IN ACTIVE GALACTIC NUCLEI: II. THE MOST LUMINOUS STANDARD CANDLES IN THE UNIVERSE

JIAN-MIN WANG^{1,5}, PU DU¹, CHEN HU¹, HAGAI NETZER², JIN-MING BAI³, KAI-XING LU⁴,
SHAI KASPI², JIE QIU¹, YAN-RONG LI¹ AND FANG WANG³
(SEAMBH COLLABORATION)

Received 2014 January 16; accepted 2014 July 29

ABSTRACT

This is the second in a series of papers reporting on a large reverberation mapping (RM) campaign to measure black hole (BH) mass in high accretion rate active galactic nuclei (AGNs). The goal is to identify super-Eddington accreting massive black holes (SEAMBHs) and to use their unique properties to construct a new method for measuring cosmological distances. Based on theoretical models, the saturated bolometric luminosity of such sources is proportional to the BH mass which can be used to obtain their distance. Here we report on five new RM measurements and show that in four of the cases we can measure the BH mass and three of these sources are SEAMBHs. Together with the three sources from our earlier work, we now have six new sources of this type. We use a novel method based on a minimal radiation efficiency to identify nine additional SEAMBHs from earlier RM-based mass measurements. We use a Bayesian analysis to determine the parameters of the new distance expression, and the method uncertainties, from the observed properties of the objects in the sample. The ratio of the newly measured distances to the standard cosmological ones has a mean scatter of 0.14 dex, indicating that SEAMBHs can be used as cosmological distance probes. With their high luminosity, long period of activity and large numbers at high redshifts, SEAMBHs have a potential to extend the cosmic distance ladder beyond the range now explored by type Ia supernovae.

Subject headings: galaxies: active – accretion, accretion disks – cosmology: observation

1. INTRODUCTION

The powerful emission of active galactic nuclei (AGN) is thought to originate from gas accretion onto supermassive black holes (BHs). In particular, a large fraction of type-I (unobscured) AGNs are powered by super-Eddington accreting massive black holes (SEAMBHs) that are characterised by a large Eddington ratio, $L_{\text{Bol}}/L_{\text{Edd}} \gtrsim 1$, where L_{Bol} is the bolometric luminosity and L_{Edd} is the Eddington luminosity (Nobuta et al. 2012; Kelly & Shen 2013; Netzer & Trakhtenbrot 2014). In the local Universe, most objects of this type are classified as narrow line Seyfert 1 galaxies (NLS1s). They have prominent features of relatively narrow broad emission lines, strong Fe II lines, weak [O III] lines, and very strong soft X-ray continuum (Osterbrock & Pogge 1985; Boller et al. 1996). SEAMBHs as central engines of NLS1s are not entirely understood. It is thought that they contain slim accretion disks where photon trapping is very important (e.g., Abramowicz et al. 1988; Wang & Zhou 1999a; Ohsuga et al. 2001).

The accelerated expansion of the Universe has been extensively studied using type Ia supernovae (SNe-Ia) (Riess et al. 1998; Perlmutter et al. 1999). Much attention has been given to improve the measurements of SNe-Ia in two directions: 1) more detections of SNe-Ia at high redshifts and 2) high accu-

racy of SNe-Ia calibrated using Cepheids (Freedman & Madore 2010; Riess et al. 2011; Freedman & Madore 2013). This method based on SNe-Ia, however, is limited to redshifts up to about $z \sim 1.5$, even for the next generation of extremely large telescopes both on the ground or in space (Hook 2012). Thus the exact dynamical state of the Universe at higher redshifts is poorly known because of the lack of reliable luminous candles (Weinberg et al. 2013; Kim et al. 2013).

The very high luminosity of AGNs makes them observable to very large distances, up to a redshift of about 7 (Mortlock et al. 2011). In principle, they could be used to follow the expansion of the early Universe, beyond the distance accessible by the SNe-Ia method. However, the diversity in their intrinsic properties (Ho 2008; Netzer 2013) hampers the use of most AGNs as distance indicators. There were several recent attempts, based on reverberation mapping (RM) of dust and gas near the central BH, to test the idea of using AGNs as standard cosmological candles. One of them makes use of the known correlation between the broad line region size (R_{BLR}) and the continuum luminosities at 5100 Å (L_{5100}) found in ~ 50 AGNs (Kaspi et al. 2000; Bentz et al. 2013; Peterson 2013). Since R_{BLR} is empirically determined by measuring the time lag between the H β line and the visual continuum, it was suggested to derive this cosmologically independent size by monitoring a large number of AGNs at various redshifts (Horne et al. 2003; Teerikorpi 2011; Watson et al. 2011; Czerny et al. 2013; Bentz et al. 2013; Melia 2014; Elvis & Karovska 2002). X-ray variability correlated with BH mass or luminosity has also been suggested to estimate cosmic distances (La Franca et al. 2014). Similarly, dust RM (correlating the variable rest frame V and K magnitudes) was suggested to measure the innermost size of the dusty “torus” as an alternative size measure (Hoenig 2014; Yoshii et al. 2014). Other suggestions involve radio megamasers (Humphreys et

¹ Key Laboratory for Particle Astrophysics, Institute of High Energy Physics, Chinese Academy of Sciences, 19B Yuquan Road, Beijing 100049, China

² Wise Observatory, School of Physics and Astronomy, Tel-Aviv University, Tel-Aviv 69978, Israel

³ Yunnan Observatory, Chinese Academy of Sciences, Kunming 650011, Yunnan, China

⁴ Astronomy Department, Beijing Normal University, Beijing 100875, China

⁵ National Astronomical Observatories of China, Chinese Academy of Sciences, 20A Datun Road, Beijing 100020, China

al. 2013), and other AGN components (see Marziani & Sulentic 2013 for a review of such methods).

The goal of this paper is to show that SEAMBHs can be used as new probes of cosmological distances provided their mass is directly measured by methods such as RM. These objects show a unique dependence of their bolometric luminosity on the BH mass (M_\bullet) which, given a proper calibration, can be used to infer cosmological distances. This idea was first introduced by Wang et al. (2013, hereafter W13) who showed that selecting SEAMBHs by the slope of their X-ray spectral energy distribution (SED, Wang et al. 2004), and estimating their BH mass using the $R_{\text{BLR}} - L_{5100}$ relation (e.g., Kaspi et al. 2000, 2005, Bentz et al. 2013) can be used to isolate a sub-group of such sources whose properties are suitable for measuring cosmological distances. However, W13 could not test their idea directly since accurate masses of SEAMBHs were not available at the time.

In 2012 we started a large RM campaign to measure BH mass in SEAMBH candidates and to identify a large enough number of such sources that can be used to establish the method and to calibrate them as standard cosmological candles. The first paper in the series (Du et al. 2014, hereafter Paper I) described our observing project that was carried out in Lijiang, China. Paper I provides detailed information about the sample selection, telescope and spectrograph, the light curves and cross correlation (CC) analysis, and the mass measurements. The observations reported in the present paper were obtained during the same observing season reported in paper-I. Their analysis revealed the presence of three confirmed SEAMBHs and one source which probably belongs to this group but with only an upper limit on the BH mass.. Combining the new confirmed SEAMBHs with the three objects reported in paper-I, and with several other SEAMBHs identified in earlier RM experiments, results in a sample which is large enough to test the idea that such objects can be used as standard cosmological candles.

The paper is arranged as follows: §2 describes various types of accretion disks in AGNs and gives the necessary approximations to estimate the accretion rate. §3 presents new RM observations and their analysis. In §4 we list the newly obtained mass and accretion rates, and explain our unique method of identifying SEAMBHs. §5 gives a full description of the new method to measure distances with SEAMBHs by way of a rigorous analysis of the errors associated with the method. In the last section we draw some conclusions regarding the merit of the new method and how can we improve it in the future.

2. AGN ACCRETION DISKS

We consider three main types of accretion flows with angular momentum onto BHs. The properties of all such flows are determined by the dimensionless accretion rate, $\dot{m} = \eta \cdot \mathcal{M}$, where $\mathcal{M} = \dot{M}_\bullet c^2 / L_{\text{Edd}}$, η is the mass-to-radiation conversion efficiency and \dot{M}_\bullet the mass accretion rate. Here \dot{m} is equivalent to the Eddington ratio defined by $L_{\text{Bol}} / L_{\text{Edd}}$, where $L_{\text{Edd}} = 1.5 \times 10^{38} (M_\bullet / M_\odot) \text{ erg s}^{-1}$ for solar composition gas.

For $\mathcal{M} \ll 1$, the accretion flow becomes advection-dominated in the radial direction and radiative cooling is inefficient and dominated by optically thin free-free emission (Narayan & Yi 1994). This situation probably applies to LINERs (Ho 2008). For small to moderate \mathcal{M} , the flow can be described as optically thick geometrically thin accretion disk, with $H/R \ll 1$, where H is the height of the disk at a radius R

(Shakura & Sunyaev 1973; hereafter SS73). In such cases, the radiative efficiency η depends on the radius of the last stable orbit which is determined by the BH spin.

Standard optically thick geometrically thin accretion disk models assume Keplerian rotation in almost perfect circular orbits and very slow inward drift velocity. Blackbody emission is very efficient at all radii and the dissipated energy is released locally (see SS73). While recent studies of thin disks show that the SED can differ, substantially, from the SS73 approximation (due to e.g., Comptonization, radiative transfer in the atmosphere, etc; Frank et al. 2002, Kato et al. 2003), none of these effects changes significantly the total energy released locally by the disk.

The SS73 model has a canonical spectrum whose (BH mass dependent) low frequency SED is given approximately by $F_\nu \propto \nu^{1/3}$. Over this part of the spectrum one can use the standard disk equations to estimate the mass accretion rate, $\dot{M}_\bullet = 0.53 (l_{44} / \cos i)^{3/2} m_7^{-1} M_\odot \text{ yr}^{-1}$ (see e.g., Frank et al. 2002; Netzer 2013), where i is the inclination angle of the accretion disk to the line of sight, $l_{44} = 4\pi d_L^2 (\lambda F_\lambda) / 10^{44} \text{ erg s}^{-1}$ and F_λ is the observed flux at $\lambda = 5100(1+z) \text{ \AA}$. The corresponding \dot{m} by the following expressions (slightly adopted from earlier works by using our preferred wavelength of 5100 \AA),

$$\dot{m}_{\text{ss}} = 20.1 \left(\frac{l_{44}}{\cos i} \right)^{3/2} m_7^{-2} \eta. \quad (1)$$

We use \dot{m}_{ss} to refer to \dot{m} derived in this way (Collin et al. 2002) and assume an averaged $\cos i \approx 0.75$ for type-I AGN. Obviously \dot{m}_{ss} and \dot{M}_\bullet require the knowledge of the distance to the object (the quantity we want to determine in this paper). This however is only required to justify that the objects we are selecting, at small redshift, are indeed SEAMBHs and the associated uncertainties do not affect much the final results since the derived distances are insensitive to the exact values of \dot{m} (see details below).

The third type of flow is the one with large \mathcal{M} . In this case, radiation pressure dominates the flow geometry at almost all radii and the disk becomes slim or thick with $H \gtrsim R$. The concept of slim disks was originally suggested by Paczynsky & Bisnovatyi-Kogan (1981) and Muchotrzeb & Paczynski (1982) to get rid of the singularity of gas density at the inner edge of the SS73 disks. Such systems have been extensively studied using vertically-averaged equations (Matsumoto et al. 1984; Muchotrzeb-Czerny 1986). Abramowicz et al. (1988) used the equations to treat slim disks as transonic flows of super-Eddington accretion onto black holes. Some of the recent studies include Szuszkiewicz et al. (1996), Beloborodov (1998), Wang & Zhou (1999a,b), Fukue (2000), Mineshige et al. (2000), Watarai & Mineshige (2001, 2013), Sadowski et al. (2011, 2013) and McKenney et al. (2013). Slim disks are characterized by sub-Keplerian rotation and transonic radial motion, which results in a non-localized energy conservation. These three properties are very different from the SS73 disks and there is no simple analytical solution except for the case of extremely high accretion rates, which can be described by a self-similar solution (Wang & Zhou 1999a; Wang & Netzer 2003).

As a result of the fast radial transportation in slim disks, most photons will be trapped and advected into the BH before escaping. This results in inefficient emission of radiation and a big reduction in η . Some models suggest that in this

TABLE 1
THE LIJIANG PROJECT: TARGETS AND OBSERVATIONS

Object	α_{2000}	δ_{2000}	redshift	monitoring period	N_{spec}	Comparison stars		Note on τ_{BLR}
						R_*	P.A.	
Mrk 335	00 06 19.5	+20 12 10	0.0258	Oct., 2012 – Feb., 2013	91	80''.7	174.5°	Yes
Mrk 1044	02 30 05.5	−08 59 53	0.0165	Oct., 2012 – Feb., 2013	77	207''.0	−143.0°	Yes
IRAS 04416+1215	04 44 28.8	+12 21 12	0.0889	Oct., 2012 – Mar., 2013	92	137''.9	−55.0°	No
Mrk 382	07 55 25.3	+39 11 10	0.0337	Oct., 2012 – May., 2013	123	198''.4	−24.6°	Yes
Mrk 142	10 25 31.3	+51 40 35	0.0449	Nov., 2012 – Apr., 2013	119	113''.1	155.2°	Yes
MCG +06−26−012	11 39 13.9	+33 55 51	0.0328	Jan., 2013 – Jun., 2013	34	204''.3	46.1°	Yes
IRAS F12397+3333	12 42 10.6	+33 17 03	0.0435	Jan., 2013 – May., 2013	51	189''.0	130.0°	Yes
Mrk 42	11 53 41.8	+46 12 43	0.0246	Jan., 2013 – Apr., 2013	53	234''.4	33.8°	No
Mrk 486	15 36 38.3	+54 33 33	0.0389	Mar., 2013 – Jul., 2013	45	193''.8	−167.0°	Yes
Mrk 493	15 59 09.6	+35 01 47	0.0313	Apr., 2013 – Jun., 2013	27	155''.3	98.5°	Yes/No

NOTE. — We include the three objects reported in paper I. N_{spec} is the numbers of spectroscopic epochs, R_* is the angular distance between the object and the comparison star and PA is the position angle from the AGN to the comparison star. The last column contains notes on the $H\beta$ time lags: “Yes” means significant lag and “No” lag could not be measured. The special case of Mrk 493 is explained in the text of the paper.

case, $\eta \propto \dot{M}^{-1}$ (Wang & Zhou 1999a; Mineshige et al. 2000; Sadowski et al. 2011). This leads to the so called “saturated luminosity” given by:

$$L_{\bullet} = \ell_0 M_{\bullet}, \quad (2)$$

where $\ell_0 = 3.0 \times 10^{38} [1 + \ln(\dot{M}/50)] \text{ erg s}^{-1} M_{\odot}^{-1}$ (Wang & Zhou 1999a; Mineshige et al. 2000). Thus $L_{\bullet} \approx 2L_{\text{Edd}}$ over a large range of accretion rates around $\dot{M} = 50$. Given an accurately measured BH mass, one can deduce L_{\bullet} and hence the BH distance provided there is a way (i.e., a reliable bolometric correction factor) to convert L_{\bullet} to the monochromatic luminosity of the disk at an accessible wavelength (see §5).

3. OBSERVATIONS REDUCTION AND CROSS CORRELATION ANALYSIS

3.1. Observations

Detailed information of our RM campaign are given in paper I where we describe the observatory, the telescope, the spectrograph and the observing procedure in great detail. In short, targets were selected from the list of SEAMBH candidates in W13 based on their coordinates and the slope of their 2–10 keV continuum requiring $\Gamma_x \geq 2.0$. All targets are classified, spectroscopically, as NLS1s i.e., 1) $\text{FWHM}(H\beta) \lesssim 2000 \text{ km s}^{-1}$; 2) $[\text{O III}]/H\beta \lesssim 3$; 3) strong Fe II emission lines. Only radio-quiet sources are selected to avoid contamination by relativistic jet emission to the optical continuum and, perhaps, emission lines⁶. The campaign started in October 2012 and lasted until June 2013. We used the Lijiang 2.4-m telescope of Yunnan Observatory, in China. We obtained optical spectra of all 10 radio-quiet selected sources almost every night with suitable weather conditions. Flux calibration is obtained through the use of a nearby comparison star that was observed in the same slit with the AGN. The variability of three of the sources (Mrk 335, Mrk 142 and IRAS F12397+3333), and their BH mass and accretion rate, was reported in paper I. Details of five additional sources, four of which were found to be SEAMBHs, are given in Table 1. Two additional radio quiet sources, that do not show significant time lags, will not be further discussed.

3.2. Host galaxy contamination

⁶ The radio-loud object 1H 0323+342 was selected by chance to be included in our observations. We detected a time lag of the $H\beta$ line relative to the 5100Å continuum and a couple of simultaneous γ -ray flares. These results will be reported separately (F. Wang, et al. 2014 in preparation).

All five targets were observed by the *Hubble Space Telescope* (HST) prior to our campaign. We use the HST images to remove the host galaxy contaminations as described in paper I. For objects with only one exposure, we use L. A. Cosmic (van Dokkum 2001) to remove cosmic rays in their images. Unlike the three other sources, Mrk 486 has only WF/PC-1 exposure with a resolution which is too low to constrain the Sérsic index of its bulge. Since a large fraction of NLS1s contain pseudo-bulges (Ryan et al. 2007; Orban de Xivry et al. 2011; Mathur et al. 2012), we fix the Sérsic index of the bulge component to 2.0. We also experimented with Sérsic indexes of 1.0 and 4.0 which changed the host flux by $\sim 10\%$, well within the uncertainty of this measurement.

The results of the fitting process are listed in Table 2 and the images are shown in Figure 1. In most cases, the host contamination, given the slit size used in the observations (2.5''), does not amount to more than $\sim 25\%$ at $5100(1+z)\text{Å}$. The uncertainty on the BH distance, \mathcal{D}_{\bullet} (see below), due to this component is $\Delta f_{\text{host}} \lesssim 5\%$, where f_{host} is the fractional contribution of the host at $5100(1+z)\text{Å}$.

3.3. Light curves and CC analysis

The various panels of figure 2 show the light curves of the five new targets and Table 4 presents the relevant measurements. We make use of the cross-correlation function (CCF) to measure the time lag of the $H\beta$ line relative to the observed continuum. The interpolated cross-correlation function (ICCF; Gaskell & Sparke 1986; Gaskell & Peterson 1987) and the Z-transformed discrete correlation function (ZDCF; Alexander 1997) methods were employed. The uncertainties of the time lags are determined using the “flux randomization (FR)/random subset sampling (RSS)” method (Peterson et al. 1998a, 2004). More details are provided in paper I. In general, we prefer the use of the 5100Å continuum for calculating the CCF. However, in one source, Mrk 382, we choose to use the better sampled V-band light curve despite the additional uncertainty due to the inclusion of several emission lines in this band.

In general, the variability we find in our hard X-ray selected NLS1 sample is different from what was found in previous monitoring of such objects where small amplitude variations in the optical bands were reported (Klimek et al. 2004). The variations are consistent with several earlier suggestions that show the variability amplitude decreases with the Eddington ratio (e.g., Zuo et al. 2012; Ai et al. 2013). These properties are important for the understanding of slim accretion disks

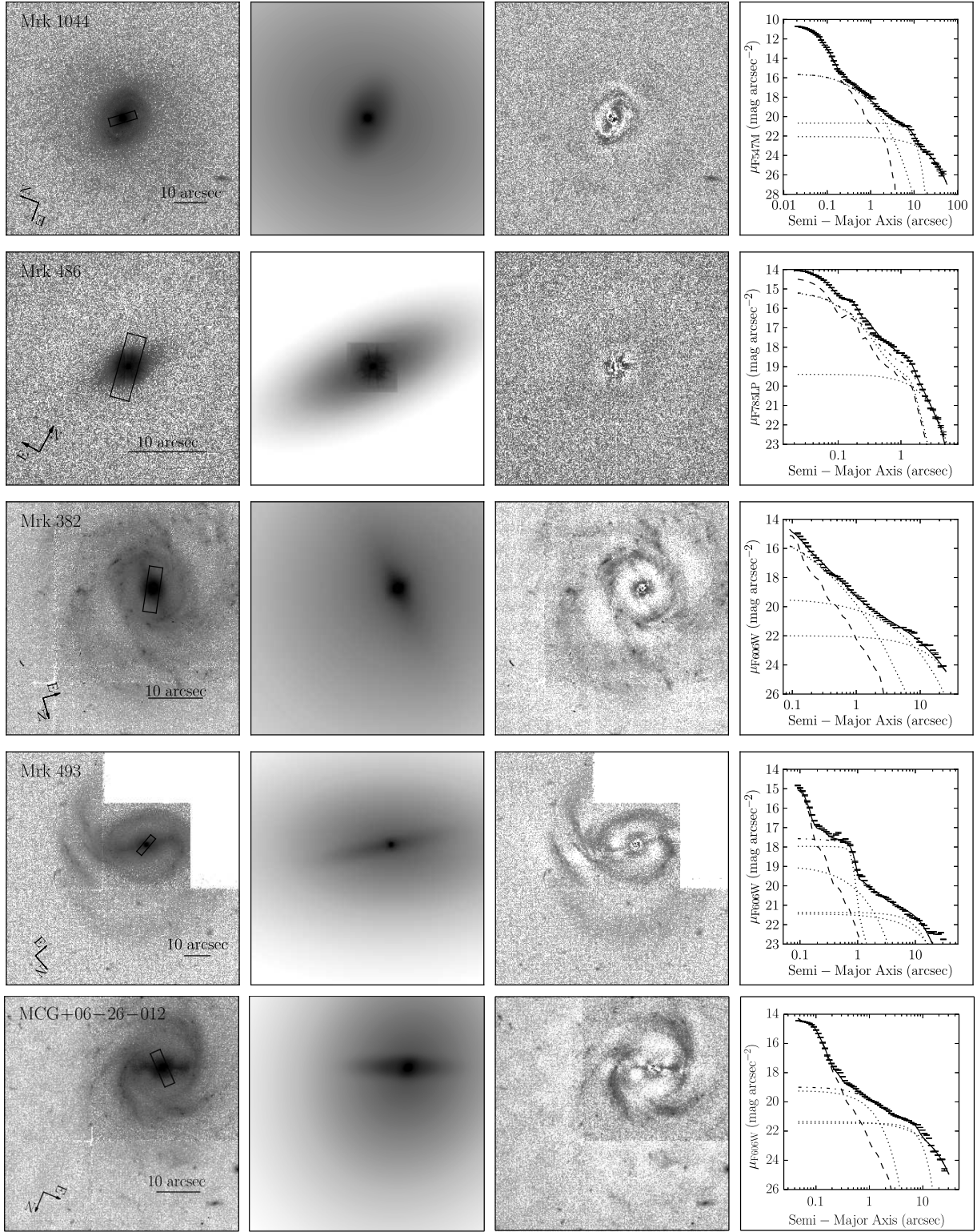


FIG. 1.— Hubble Space Telescope images of Mrk 1044, IRAS F12397+3333, Mrk 486, Mrk 493 and MCG +06-26-012. The left panels show the original images and the small boxes illustrate the spectroscopic aperture used to extract the spectrum. The 2nd column shows model images, the 3rd one the residuals obtained after subtracting the fitted model. The 4th column shows one-dimensional surface profiles of the three galaxies. Points with error bars are observed data, solid lines are the best-fit models, dashed lines are PSFs, dash-dotted lines are host profiles and dotted lines are the components (Sérsic profiles) used to model the host galaxy light.

and will be discussed in detail in future publications.

3.4. Notes on individual sources

Mrk 1044: *ROSAT* observations show evidence for soft X-ray variability of this source (Boller et al. 1996). Our CCF analysis shows a peak at ~ 5 days with a maximum

TABLE 2
HOST GALAXY DECOMPOSITION

Object	Data set	Observational setup	m_{st}^*	R_e (")	n	b/a	P.A. (deg)	Note	χ^2_ν
Mrk 486	W0MT010	WFPC, P6, F785LP	16.69 ± 0.01					PSF	1.278
			16.46 ± 0.01	0.11	[2.0]	0.66 ± 0.01	-45.73 ± 1.04	Bulge	
			16.75	2.41	[1.0]	0.41	-37.28 ± 0.24	Disk	
			0.032					Sky	
Mrk 382	U2E62I01T	WFPC2, PC1, F606W	17.16					PSF	1.068
			16.77	0.51	3.34 ± 0.03	0.83	-64.65 ± 0.42	Bulge	
			16.25 ± 0.02	6.98 ± 0.07	1.70 ± 0.02	0.41	7.38 ± 0.07	Bar	
			14.82 ± 0.01	18.5 ± 0.11	[1.0]	0.96	-43.38 ± 3.52	Disk	
MCG +06	U2E61L01T	WFPC2, PC1, F606W	0.023					Sky	0.761
			18.22					PSF	
			18.43	0.07	0.35 ± 0.01	0.41	24.10 ± 0.28	Add'l PSF	
			18.09	1.02	0.81	0.82	-35.23 ± 0.52	Bulge	
Mrk 493	U2E62O01T	WFPC2, PC1, F606W	17.05	6.48 ± 0.01	0.41	0.27	-67.93 ± 0.04	Bar	1.191
			14.69	15.4 ± 0.02	[1.0]	0.85	1.47 ± 0.18	Disk	
			0.019					Sky	
			17.34					PSF	
Mrk 1044	IBGU10	WFC3, UVIS1, F547M	17.26	0.59	0.11	0.83	-38.13 ± 0.24	N. Spiral/Ring	1.160
			17.42	1.52	1.18 ± 0.02	0.85	49.24 ± 0.62	Bulge	
			16.23	11.4 ± 0.01	0.57	0.21	60.24 ± 0.02	Bar	
			14.72	19.4 ± 0.02	[1.0]	0.57	48.41 ± 0.05	Disk	
Mrk 1044	IBGU10	WFC3, UVIS1, F547M	0.015					Sky	1.160
			15.35					PSF	
			15.71	0.85	1.86	0.98	-87.24 ± 0.07	Bulge	
			15.38	6.33	0.41	0.65	87.63 ± 0.08	Bar	
Mrk 1044	IBGU10	WFC3, UVIS1, F547M	14.70	21.2 ± 0.11	[1.0]	0.87	-3.48 ± 0.50	Disk	1.160
			0.011					Sky	

NOTE. — The values in square brackets are fixed in the fitting procedure. m_{st}^* is the ST magnitude, an f_λ -based magnitude system, $m_{\text{ST}} = -2.5 \log_{10}(f_\lambda) - 21.10$, for f_λ in $\text{erg s}^{-1} \text{cm}^{-2} \text{\AA}^{-1}$ (see Sirianni et al. 2005). The units of sky are electrons/s. Note that only errors that exceed a certain value are listed by GALFIT and cases without error bars mean an uncertainty below this limit.

cross-correlation coefficient of $r_{\text{max}} \approx 0.55$. The measured M_\bullet combined with the conservative assumption on the spin give $\dot{m}_{\text{min}} \sim 2.73$, the largest in our sample.

Mrk 382: This object shows the strongest host contamination in our sample. Because of this, the 5100Å flux calibration is uncertain and we chose to use the V-band light curve, with their improved precision, in the CCF analysis (the only source in our sample). Using the entire light curve we obtain a peak correlation of $r_{\text{max}} = 0.49$ and a time lag of $\tau = 5.8^{+1.6}_{-1.5}$ days. Since the first part of the observations of this object suffers from bad-weather and problems with continuum subtraction from the H β line, this resulted in a noisier light curve in the first part of the campaign. Thus, we also analyzed only the second half of the light curve, with its improved sampling (blue points in Figure 2). This gives a stronger correlation with $r_{\text{max}} = 0.65$ corresponding to a time lag of $\tau = 6.6^{+1.1}_{-0.7}$ days in the rest frame of the source. In the following analysis we use this time lag.

Mrk 486: The source shows significant flux and SED variations in the X-ray band (Ballo et al. 2008). The gap in the data between JD260-290 (see Figure 2) is due to bad weather. The H β light curve shows a monotonic decreases with time and much of the signal in the CCF is due to the flux increase at the end of the campaign, on July 14 and 15, 2013. The observations on those night were taken under very good conditions and we have no reason to suspect these measurements.

Mrk 493: We obtained only 27 observations from April to June 2013. This makes the quality of the CCF poorer than in other objects and results in a larger uncertainty on the time lag which is consistent with zero (although the peak of the CCF is very clear with $r_{\text{max}} \sim 0.54$). We report on the various results obtained for this source but do not include it in the distance analysis.

MCG +06-26-012: This NLS1 is situated in a Sb galaxy (see *HST* image in Figure 1). We find $\text{FWHM}(\text{H}\beta) = 1685 \text{ km s}^{-1}$ (see also Grupe et al. 1999; Veron-Cetty et al. 2001). The CCF shows a statistically significant time lag of $\tau_{\text{BLR}} = 23.3^{+7.5}_{-5.8}$ days with $r_{\text{max}} \approx 0.9$. From Eqn. (3), we get $M_\bullet = (8.3^{+2.9}_{-2.3}) \times 10^6 M_\odot$. The host-galaxy subtracted luminosity is $L_{5100} = (0.47 \pm 0.10) \times 10^{43} \text{ erg s}^{-1}$. Using our method to determine accretion rate [Eqn. (4) below] we get $\dot{m}_{\text{min}} = 0.02$, indicating that this object is not a SEAMBH.

Finally we comment on the general method of measuring line intensities in this and earlier RM experiments. The H β light curves reported here and in paper I were obtained by simple integration over the line profile using a locally determined continuum. These are not necessarily the most accurate light curves and spectral fitting methods that include other components, such as the host galaxy SED and the Fe II lines (e.g., Barth et al. 2013) can lead to significant improvements and reduced uncertainties. In some rare cases, this can also be used to recover points in the light curve that were discarded due to poor weather conditions that prevented us from using the local comparison star as our flux calibrator. We are working on the improvement of such methods and will report the results in a future publication (Hu et al. in preparation).

4. SUPER-EDDINGTON ACCRETING MASSIVE BLACK HOLES

4.1. Black hole mass measurements

Measuring BH mass through RM is a well established method. It is based on the idea that the velocities of the clouds emitting the broad emission lines are virialized in the BH gravitational potential and the emitted line intensities echo the variable ionizing continuum. The time-lag, τ_{BLR} , reflects the size and geometry of the variable part of the BLR and the emissivity weighted radius is given by $R_{\text{BLR}} = c\tau_{\text{BLR}}$, where

TABLE 3
CONTINUUM AND H β LIGHT CURVES

Mrk 1044			Mrk 382			MCG +06−26−012			Mrk 486			Mrk 493			
JD	F_{5100}	$F_{H\beta}$	JD	V	JD	$F_{H\beta}$	JD	F_{5100}	$F_{H\beta}$	JD	F_{5100}	$F_{H\beta}$	JD	F_{5100}	$F_{H\beta}$
29.3	5.35 ± 0.08	3.82 ± 0.02	24.4	-0.074 ± 0.008	24.4	0.41 ± 0.01	115.3	0.55 ± 0.01	0.37 ± 0.01	179.4	3.54 ± 0.03	3.45 ± 0.01	201.4	1.80 ± 0.01	1.03 ± 0.01
31.3	4.93 ± 0.03	3.77 ± 0.02	25.4	-0.007 ± 0.009	25.4	0.40 ± 0.01	117.3	0.55 ± 0.01	0.39 ± 0.01	181.4	3.55 ± 0.08	3.49 ± 0.02	202.4	1.76 ± 0.02	1.00 ± 0.01
36.2	4.89 ± 0.01	3.76 ± 0.01	26.4	-0.021 ± 0.006	26.4	0.40 ± 0.01	152.4	0.56 ± 0.01	0.34 ± 0.01	185.4	3.48 ± 0.02	3.41 ± 0.01	203.4	1.75 ± 0.01	1.00 ± 0.01
39.2	5.40 ± 0.03	3.79 ± 0.01	27.4	-0.012 ± 0.005	27.4	0.37 ± 0.01	153.4	0.56 ± 0.01	0.33 ± 0.01	186.4	3.57 ± 0.05	3.55 ± 0.03	204.4	1.74 ± 0.01	1.01 ± 0.01
41.2	5.53 ± 0.02	3.92 ± 0.01	28.3	-0.022 ± 0.012	28.3	0.39 ± 0.01	172.3	0.66 ± 0.01	0.37 ± 0.01	190.4	3.46 ± 0.05	3.56 ± 0.01	206.4	1.72 ± 0.01	1.00 ± 0.01

NOTE. — The full version of this table is also available in machine-readable form in the electronic version of the *Astrophysical Journal*. JD: Julian dates from 2456200; F_{5100} and $F_{H\beta}$ are fluxes at $(1+z)5100\text{\AA}$ and H β emission line in units of $10^{-15} \text{ erg s}^{-1} \text{ cm}^{-2} \text{\AA}^{-1}$ and $10^{-13} \text{ erg s}^{-1} \text{ cm}^{-2}$, respectively. V is V-band instrumental magnitude. The systematic uncertainties of F_{5100} and $F_{H\beta}$ (see paper I) are $(\Delta F_{5100}, \Delta F_{H\beta}) = (0.163, 0.056), (0.018, 0.017), (0.049, 0.052)$ and $(0.045, 0.025)$ for Mrk 1044, MCG 06, Mrk 486 and Mrk 493 respectively. $\Delta F_{H\beta} = 0.016$ for Mrk 382. Since the space limitation, effective numbers of JD and fluxes have been cut down in this Table, however they four effective numbers, all others have three, respectively, in the electronic version.

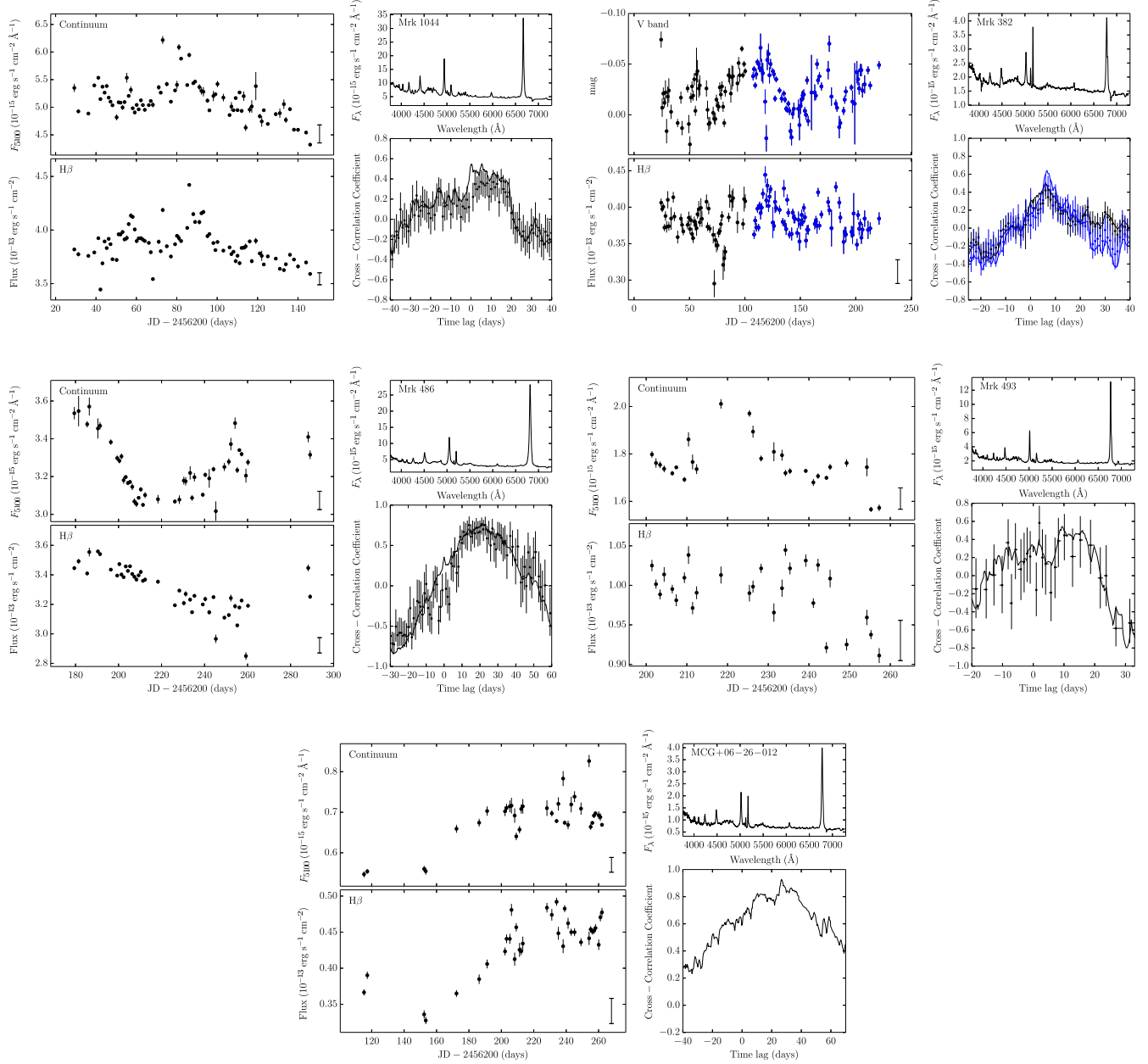


FIG. 2.— Light curves and CCF analysis. The *left* panels show light curves of H β and F_{5100} (V-band in Mrk 382). The *right* panels show mean spectra and cross-correlation functions. For Mrk 382, we divided the light curves into two parts shown by blue and black points. The black CCFs are obtained from the entire light curves while the blue one from the blue light curves. The parts of the light curves shown by blue points result in a more significant time lag which is the one listed in Table 1.

c is the speed of light. RM experiments provide the necessary measurements of R_{BLR} which, combined with the viri assumption, result in a simple expression for the BH mass,

$$M_{\bullet} = f_{\text{BLR}} \frac{V_{\text{BLR}}^2 R_{\text{BLR}}}{G}, \quad (3)$$

where G is the gravitational constant, V_{BLR} is a measure of the gas velocity, and f_{BLR} is a constant which combines all the unknowns about the geometry and kinematics of the gas in the BLR. The best value of f_{BLR} is obtained by using BH mass estimated determined by the $M_{\bullet} - \sigma_{*}$ relationship in AGNs where stellar absorption features can be observed (Woo et al. 2013).

We have used our observations to measure the mass of the BHs in our sample through Eqn. (3). In principle there are four possible choices to define V_{BLR} (e.g., Collin et al. 2006): 1) the full-width-at-half-maximum (FWHM) of the variable component of the line obtained from the RMS spectrum (Peterson et al. 1998b; Wandel et al. 1999), 2) the FWHM of the line obtained from the mean spectrum (e.g., Kaspi et al. 2000), 3) the line dispersion (so called σ_{line}) obtained from the rms spectrum (e.g., Fromerth & Melia 2000; Peterson et al. 2004; Collin et al. 2006; Denney et al. 2013) and 4) the line dispersion obtained from the mean spectrum (e.g., Collin et al. 2006; Bian et al. 2008). For example, the recent Woo et al. (2013) work suggests that for σ_{line} measured from the rms spectrum, $f_{\text{BLR}} \simeq 5.3$. Despite many years of study, there is no empirical evidence, or a realistic model, to show that any of the methods is preferred over the others.

Following paper I, we have chosen to use the FWHM(H β) from the mean spectrum as our choice of V_{BLR} . Applying this to the Woo et al. (2013) sample of 25 AGNs with measured σ_{*} gives $f_{\text{BLR}} = 1.00 \pm 0.25$ (Woo, private communication) with no dependence on BH mass or accretion rate. The scatter in the derived M_{\bullet} obtained in this way is very similar to the scatter observed by assuming $V_{\text{BLR}} = \sigma_{\text{line}}$ with its corresponding f_{BLR} . Our measurements of M_{\bullet} based on this method are listed in Table 4 and more references regarding this choice are provided in paper I.

4.2. Identifying SEAMBHs by their accretion rates

The SEAMBHs discussed in this work belong to the category of slim accretion disks. They can be recognized by their \dot{m} that approaches and even exceeds unity. However, the uncertainties on present slim disk models, and the uncertainties on the observations, are too large to identify a specific value of \dot{m} beyond which photon trapping is significant. Various models (Laor & Netzer 1989; Beloborodov 1998; Sadowski et al. 2011) suggests that this occurs at $\dot{m} \simeq 0.1 - 0.3$ but even this range is uncertain.

Returning to SEAMBHs with higher accretion rate, we note that the value of \dot{m} which is required to identify such objects can be determined from the measured M_{\bullet} and the global SED of the disk. However, we do not have access to the entire SED because of the Galactic and intergalactic absorption. We can only estimate the mass accretion rates, \dot{M}_{\bullet} , from the observed optical continuum and the results of the existing slim disk models that suggest this to be a good approximation since the wavelengths used correspond to the parts of the disk that are not affected by photon trapping. The uncertainty on BH spin, and \mathcal{M} and η still remains.

To overcome the uncertainty related to the BH spin, we adopted a conservative approach that uses the smallest possi-

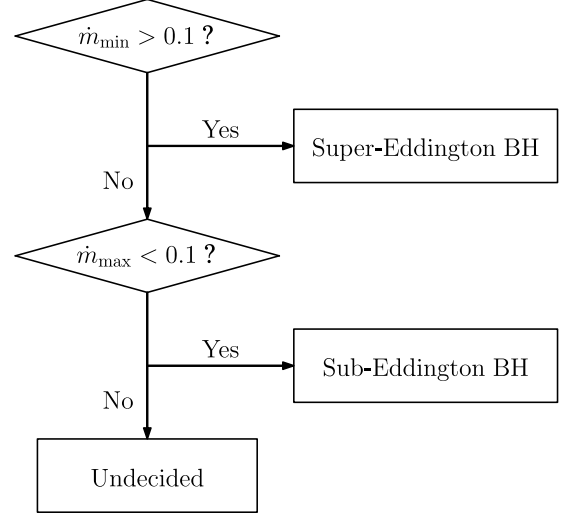


FIG. 3.— Flow chart used to identify SEAMBHs. The undecided category is for sources with not enough information on \dot{m} to decide whether they are powered by thin or slim disks.

ble \dot{m} based on the smallest possible η . For a maximally rotating pro-grade disk ($a = 0.998$), the radiative efficiency reaches its maximum of $\eta_{\text{max}} = 0.32$. From Eqn. (1), the maximum accretion rate assuming $\cos i = 0.75$ is $\dot{m}_{\text{max}} = 9.9 l_{44}^{3/2} m_7^{-2}$. If $\dot{m}_{\text{max}} \leq 0.1$, this object has too low accretion rate to maintain a slim disk. In the same way we define a minimum accretion rate, \dot{m}_{min} by using the lowest possible $\eta_{\text{min}} = 0.038$ corresponding to a retrograde spinning BH with $a = -1$,

$$\dot{m}_{\text{min}} = 1.2 l_{44}^{3/2} m_7^{-2}. \quad (4)$$

If $\dot{m}_{\text{min}} \geq 0.1$, the disk must be slim, and the object is considered to be a SEAMBH. Obviously there are objects with $\dot{m}_{\text{min}} < \dot{m} < \dot{m}_{\text{max}}$ which we do not consider SEAMBHs by our very conservative criterion, that may be powered by slim accretion disks if η is large enough. We can introduce an even more conservative criterion by combining \dot{m}_{min} and \dot{m}_{max} . Since $\dot{m}_{\text{min}} = (\eta_{\text{min}}/\eta_{\text{max}}) \dot{m}_{\text{max}} \approx 0.12 \dot{m}_{\text{max}}$, we get $\dot{m}_{\text{min}} \geq 0.12$ for SEAMBHs with $\dot{m}_{\text{max}} \geq 1$. In the present paper we use $\dot{m}_{\text{min}} \geq 0.1$ as the only criterion.

A flow chart diagram for identifying SEAMBHs is given in Figure 3. Applying Eqn. (4) to our sample we find 7 targets (the three from paper I and four from this work) to have slim accretion disks. As explained earlier, we decided not to use Mrk 493 because of the large uncertainty on the time lag and hence the BH mass. All together, six of the new objects are suitable for the distance analysis. It is interesting to note that the fraction of SEAMBHs from our targets reaches $\sim 70\%$ suggesting that the Γ_{2-10} -based selection is very efficient for identifying SEAMBH candidates.

We used the same method to search for SEAMBHs among the entire sample (~ 40) of radio-quiet AGNs with previous RM-based BH mass measurements (Peterson et al. 1998a; Kaspi et al. 2000, 2005; Bentz et al. 2013). We found 9 objects with $\dot{m}_{\text{min}} > 0.1$. Thus the total number of newly identified SEAMBHs with directly measured BH mass and $\dot{m}_{\text{min}} > 0.1$, is 15 under the most conservative assumption about the BH spin. We also found 21 objects with $\dot{m}_{\text{max}} < 0.1$, which must be powered by thin disks. The rest of the sources have $\dot{m}_{\text{min}} < \dot{m} < \dot{m}_{\text{max}}$. Obviously the real number of ob-

TABLE 4
SEAMBHS: MASSES AND ACCRETION RATES

Objects	τ_{BLR} (days)	FWHM (km s ⁻¹)	M_{\bullet} (10 ⁶ M_{\odot})	\dot{m}_{min}	$F_{\lambda}[(1+z)5100]$ (10 ⁻¹⁵ erg s ⁻¹ cm ⁻²)	$E(B-V)$	\mathcal{D}_{L} (Mpc)	\mathcal{D}_{\bullet} (Mpc)
SEAMBHS identified by the Shangri-La campaign								
Mrk 335	10.6 ^{+1.7} _{-2.9}	1997 ± 265	8.3 ^{+2.6} _{-3.2}	0.60 ^{+1.13} _{-0.29}	5.20 ± 0.37	0.030	117.6	85.9 ^{+21.5} _{-26.3}
Mrk 1044	4.8 ^{+7.4} _{-3.7}	1211 ± 48	1.4 ^{+2.1} _{-1.1}	2.73 ^{+60.63} _{-2.38}	3.28 ± 0.37	0.031	74.5	31.4 ^{+32.2} _{-20.8}
Mrk 382	6.6 ^{+1.1} _{-0.7}	1588 ± 330	3.3 ^{+1.5} _{-1.4}	0.54 ^{+1.55} _{-0.34}	0.78 ± 0.13	0.043	154.5	114.2 ^{+47.4} _{-42.4}
Mrk 142	6.4 ^{+0.8} _{-2.2}	1647 ± 69	3.4 ^{+0.5} _{-1.2}	2.25 ^{+4.11} _{-0.84}	1.27 ± 0.15	0.015	207.9	95.5 ^{+16.4} _{-28.6}
IRAS F12397	11.4 ^{+2.9} _{-1.9}	1835 ± 473	7.5 ^{+4.3} _{-4.1}	0.51 ^{+2.27} _{-0.33}	1.44 ± 0.14	0.017	201.0	154.5 ^{+67.8} _{-68.4}
Mrk 486	20.0 ^{+8.7} _{-3.2}	1926 ± 157	14.5 ^{+6.7} _{-3.3}	0.19 ^{+0.17} _{-0.11}	2.34 ± 0.17	0.012	179.3	192.8 ^{+67.9} _{-37.3}
Mrk 493	12.2 ^{+3.5} _{-16.7}	784 ± 11	1.5 ^{+0.4} _{-1.5}	> 1.23	0.94 ± 0.13	0.022	143.5	62.0 ^{+17.4} _{-62.0}
SEAMBHS identified from sources mapped by previous campaigns								
Mrk 110	24.3 ^{+5.5} _{-8.3}	1543 ± 5 ^a	11.3 ^{+2.6} _{-3.9}	0.30 ^{+0.43} _{-0.11}	2.79 ± 0.09	0.011	162.1	149.2 ^{+25.1} _{-39.0}
Mrk 202	3.0 ^{+1.7} _{-1.1}	1471 ± 18 ^b	1.3 ^{+0.7} _{-0.5}	0.17 ^{+0.46} _{-0.13}	0.30 ± 0.11	0.018	95.5	100.8 ^{+62.3} _{-36.1}
NGC 4051	1.9 ^{+0.5} _{-0.5}	1453 ± 3 ^a	0.8 ^{+0.2} _{-0.2}	0.17 ^{+0.24} _{-0.10}	4.93 ± 1.00	0.011	17.1	17.9 ^{+5.7} _{-4.6}
NGC 7469	24.3 ^{+4.0} _{-4.0}	1722 ± 30 ^a	14.1 ^{+2.4} _{-2.4}	0.17 ^{+0.11} _{-0.06}	10.80 ± 1.00	0.061	73.9	82.4 ^{+13.9} _{-13.0}
PG 0026+129	111.0 ^{+24.1} _{-28.3}	2544 ± 56 ^a	140.3 ^{+31.1} _{-36.3}	0.17 ^{+0.15} _{-0.06}	2.31 ± 0.07	0.063	700.4	829.9 ^{+136.1} _{-163.9}
PG 0844+349	32.3 ^{+13.7} _{-13.4}	2694 ± 58 ^a	45.8 ^{+19.5} _{-19.1}	0.12 ^{+0.32} _{-0.07}	2.57 ± 0.38	0.033	300.0	390.3 ^{+151.8} _{-139.9}
PG 1211+143	93.8 ^{+25.6} _{-42.1}	2012 ± 37 ^a	74.2 ^{+20.4} _{-33.4}	0.26 ^{+0.86} _{-0.14}	5.06 ± 0.92	0.030	383.6	386.8 ^{+119.0} _{-151.4}
PG 1700+518	251.8 ^{+45.9} _{-38.8}	2252 ± 85 ^a	249.5 ^{+49.2} _{-42.8}	0.45 ^{+0.22} _{-0.14}	1.86 ± 0.03	0.030	1565.9	1358.1 ^{+188.1} _{-171.9}
PG 2130+099	31.0 ^{+4.0} _{-4.0}	2450 ± 188 ^c	36.3 ^{+7.3} _{-7.3}	0.18 ^{+0.11} _{-0.06}	2.53 ± 0.09	0.039	295.0	332.8 ^{+50.9} _{-52.0}

NOTE. — All measurements of Mrk 335, Mrk 142 and IRAS F12397 are from paper I. The other objects of the campaign are from this work. *a*: FWHM is from Collin et al. (2006); *b*: FWHM from Bentz et al. (2009a); *c*: FWHM from Grier et al. (2012). $F_{\lambda}[(1+z)5100]$ is obtained from the mean spectrum after the subtraction of the host galaxy contribution. For the previous campaigns, we use the values of $F_{\lambda}[(1+z)5100]$ and τ_{BLR} corrected by Bentz et al. (2009ab) and Bentz et al. (2013). $E(B-V)$ is the Galactic extinction using the maps in Schlafly et al. (2011). All listed values of d_{L} are obtained from the redshift using standard cosmology (Ade et al. 2013) except for NGC 4051 where the redshift is very small and a more reliable value of $d_{\text{L}} = 17.1$ Mpc is obtained from the Tully-Fisher relation (Bentz et al. 2013). The error on d_{L} is assumed to be 2% in all sources (see text). The errors on d_{\bullet} are from the calculations of Δ_{obs} (the combination of the errors on F_{5100} , FWHM and τ_{BLR}). Note that the mass and distance calculated for Mrk 493 are consistent with zero and hence this source is not used in the distance analysis.

jects containing slim disks could be larger, but because of our conservative estimate of \dot{m} , we have no way to prove it. The uncertainty on \dot{m}_{min} is obtained from the uncertainty on \dot{M} that includes the measured flux, the BH mass and the inclination to the line-of-sight. The uncertainty due to inclination is discussed below.

5. THE COSMOLOGICAL DISTANCE OF SEAMBHS

5.1. Basic equations

To measure the distance from L_{\bullet} using the new method we have to know the bolometric correction factor defined by $\kappa_{\text{Bol}} = L_{\bullet}/L_{5100}$, where L_{5100} is the luminosity at 5100Å. Ideally, this could be determined by direct observations and integration over the entire SEDs. As explained, this is not possible in the UV and EUV parts of the spectrum and hence this is normally replaced by an empirical estimate of κ_{Bol} such as the one calculated by Marconi et al. (2004). For geometrically thin disks, $\kappa_{\text{Bol}} \propto (\dot{M}/M_{\bullet})^{1/3}$ (Frank et al. 2002). As demonstrated by Netzer & Trakhtenbrot (2014), the difference between these two approximations can be very large. The situation regarding slim disks is even more problematic since models of such objects are rather uncertain which reflects on the uncertainty in κ_{Bol} .

The approach adopted here is to use the simple slim disk calculation (Abramowicz et al. 1988) to write a generic approximation for κ_{Bol} and use the observations to find the pa-

rameters in this equation. The expression is motivated by thin disk models and is given by

$$\kappa_{\text{Bol}} = \kappa_0 m_7^{-\beta}, \quad (5)$$

where $m_7 = M_{\bullet}/10^7 M_{\odot}$. For the simplest slim disks $\kappa_0 = 40$ and $\beta = 1/3$ (Mineshige et al 2000; see also Wang et al. 1999b, Shimura & Manmoto 2003).

Having defined the bolometric correction term, we define F_{5100} as the measured λF_{λ} at $\lambda = 5100(1+z)$ Å, after correcting for foreground extinction. Thus, $\mathcal{D}_{\bullet} = (\xi L_{\bullet}/4\pi\kappa_{\text{Bol}}F_{5100})^{1/2}$, where ξ is the radiation anisotropy factor which is a complex function of the disk geometry and inclination angle i (e.g Madau 1988). We approximate this by $\xi = \cos i/0.5$ for a thin disk and by $\xi = 1$ for a thick disk. For slim disks in type-I AGNs, $\cos i \simeq 0.75$ and $H/R \lesssim 1$ so $\xi \approx 1$ is a good approximation. We can now combine ℓ_0 , ξ and κ_0 into one parameter,

$$\ell_{\kappa} = \xi \ell_0 / \kappa_{40}, \quad (6)$$

where $\kappa_{40} = \kappa_0/40$. This result in the final expression for the distance:

$$\mathcal{D}_{\bullet} = 250.3 \ell_{\kappa}^{1/2} m_7^{(1+\beta)/2} F_{11}^{-1/2} \text{ Mpc}, \quad (7)$$

where $F_{11} = F_{5100}/10^{-11} \text{ erg s}^{-1} \text{ cm}^{-2}$.

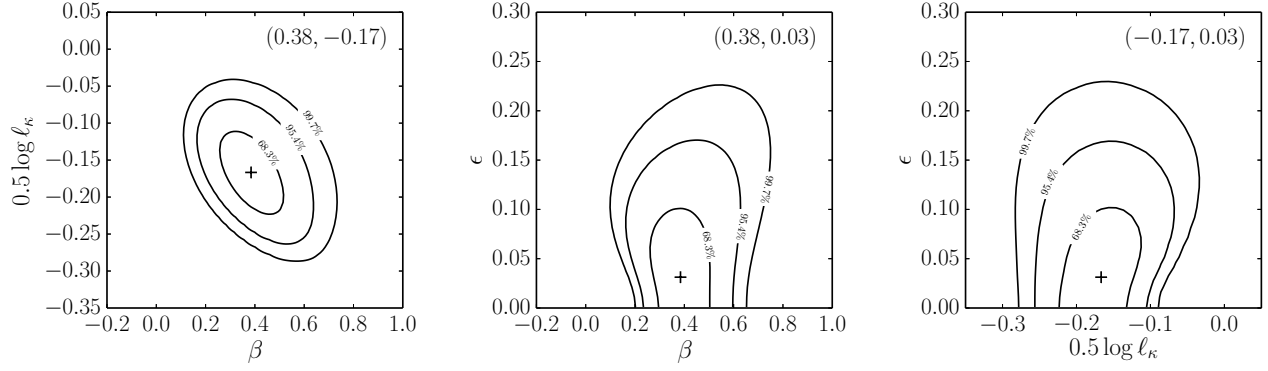


FIG. 4.— Significant level contours. *Left, middle and right* panels show $(\log \ell_\kappa - \beta)$, $(\epsilon - \beta)$ and $(\epsilon - \log \ell_\kappa)$, respectively. Levels of significance are marked on the contour lines.

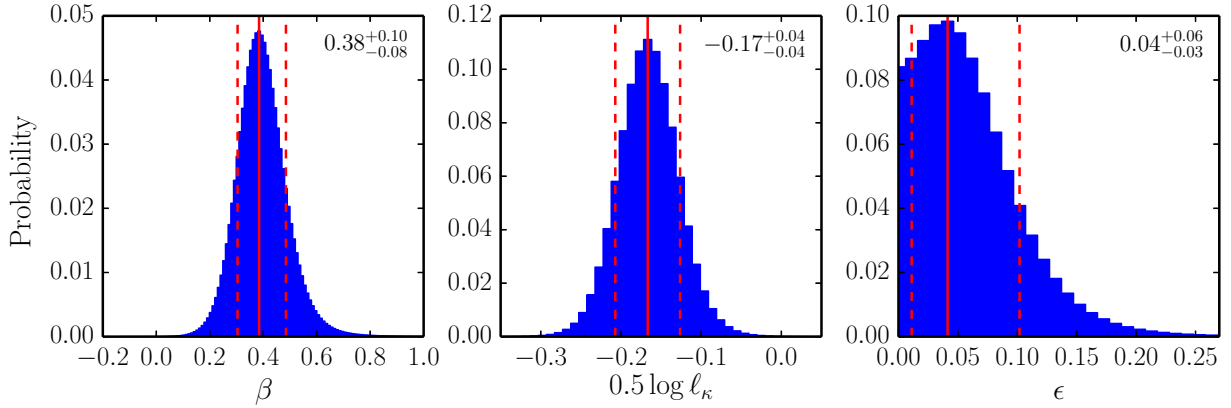


FIG. 5.— The calculated probabilities of $\log \ell_\kappa$ (left), β (middle) and ϵ (right).

5.2. Error estimate and model uncertainties

To understand the various uncertainties associated Eqn. (7), we divide all the variables contributing to the error on the distance into three different groups. The first group contains three measurable quantities, the continuum flux F_{5100} , the velocity V_{BLR} and time lag τ_{BLR} that are used to calculate the mass (the uncertainty on the host galaxy flux is included in the uncertainty on F_{5100}). These uncertainties are listed in Table 4. The second group contains f_{BLR} which is not measured in individual sources but derived from the known properties of RM AGNs with host that show absorption lines. As explained, we use the Woo et al. (2013 and private communication) result of $f_{\text{BLR}} = 1.00 \pm 0.25$. In particular we use $\Delta \log f_{\text{BLR}} = 0.07$.

The third group includes parameters that can in principle be obtained from the slim disk theory. For the simplified slim disk model used here these are ℓ_0 , ξ and κ_{Bol} that are all absorbed into ℓ_κ (Eqn. 6). The anisotropy factor, ξ , is a complicated function of the disk geometry and include the effects of radiative transfer, inclination, reflection by the funnel walls, etc. As explained, the approximation adopted here is $\xi = 1$ with an uncertainty similar to the uncertainty on $\cos i$. For type-I AGNs, the inclination angle i can change over a small range of $\cos i = 0.5 - 1$. With our chosen value of $\cos i = 0.75$ we get $\Delta \cos i / \cos i \simeq 0.33$ and $\Delta \log \xi = 0.07$.

The total uncertainty on a given \mathcal{D}_\bullet is obtained by combining the uncertainties associated with the BH mass measure-

ments and the flux, with those estimated for ξ and f_{BLR} and are assumed to be the same for all objects. This should also be combined with the uncertainty on ℓ_κ which cannot be obtained directly from the simple disk model and hence required different considerations. As we show below, the remaining uncertainties and the missing constant of calibration, can be obtained by a comparison with the observations.

5.3. Distance Calibration

We define $d_\bullet = \log \mathcal{D}_\bullet$ and write eqn. 7 for source i as

$$d_\bullet = c_0 + \ell + (1 + \beta)m_i - F_i + \epsilon_i, \quad (8)$$

where $c_0 = \log 250.3 = 2.398$, $m_i = \frac{1}{2} \log m_7$, $F_i = \frac{1}{2} \log F_{11}$ and $\ell = \frac{1}{2} \log \ell_\kappa$ (same for all sources). The new term, ϵ_i , is the intrinsic scatter associated with the new method. It represents the uncertainty related to additional physical parameters that were not included in our simple slim disk model (e.g., BH spin). If such terms are important, they will introduce a large scatter which will dominate the uncertainty in d_\bullet . We assume that ϵ_i has a Gaussian distribution with a $1-\sigma$ width of ϵ .

The calibration of ℓ and β is achieved by requiring that $\mathcal{D}_\bullet = \mathcal{D}_L$, where \mathcal{D}_L is the luminosity distance derived from the standard cosmological model. For low redshift sources, the uncertainty on \mathcal{D}_L is equivalent to the uncertainty on H_0 which is less than 2% (Freedman & Madore 2013). This is significantly smaller than the uncertainties on \mathcal{D}_\bullet (see Ta-

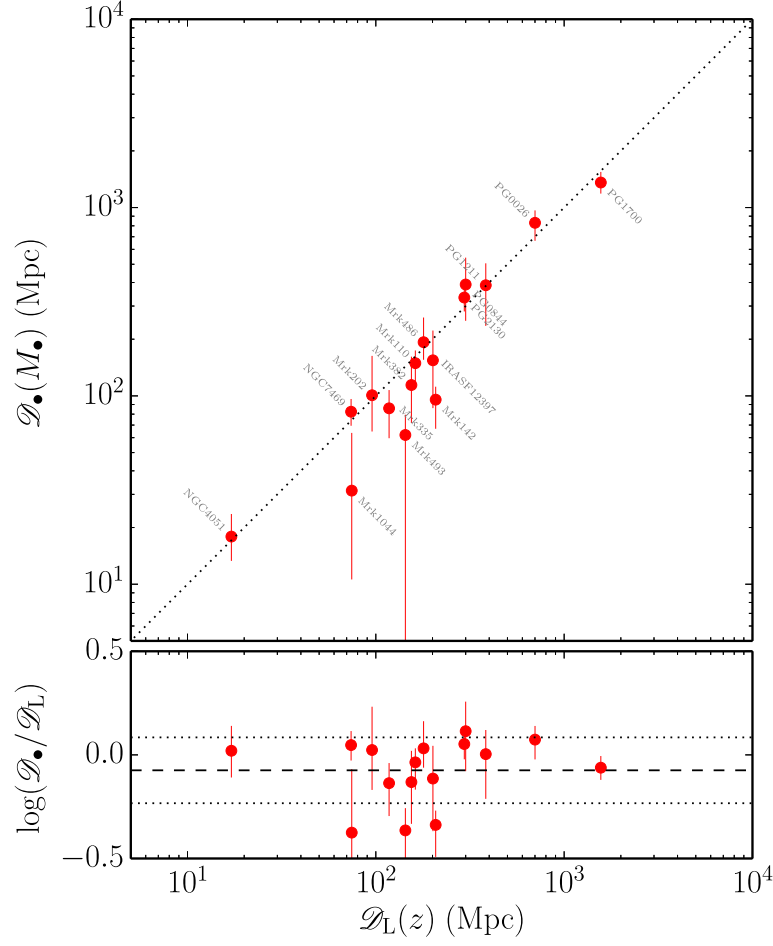


FIG. 6.— Comparison of the newly derived distances, \mathcal{D}_\bullet , with those obtained from the standard cosmological model. The dotted line in the upper panel is $\mathcal{D}_\bullet = \mathcal{D}_L$ and the dashed line in the bottom panel indicates the mean values of $\log \mathcal{D}_\bullet / \mathcal{D}_L^i$ is -0.06 , in our sample. The error bars are those listed in Table 4.

ble 4) and we do not include this in our Bayesian analysis. The values of cosmological parameters chosen here are based on the recent Planck measurements (Ade et al. 2013): $H_0 = 67 \text{ km s}^{-1} \text{ Mpc}^{-1}$, $\Omega_M = 0.32$ and $\Omega_\Lambda = 0.68$ (note that the use of H_0 only is not enough since the redshift range is $0-0.3$).

Using Bayes' theorem, the posterior probability is

$$p(\ell, \beta, \epsilon | \{m_i, F_i\}) \propto p(\{m_i, F_i\} | \ell, \beta, \epsilon) \times p(\ell, \beta, \epsilon), \quad (9)$$

where $p(\{m_i, F_i\} | \ell, \beta, \epsilon)$ is the likelihood function and $p(\ell, \beta, \epsilon)$ is the prior probability. Since the error distributions of $\{m_i, F_i\}$ are not Gaussian, we employ asymmetric Gaussians to approximate their distributions. The function $p(\ell, \beta, \epsilon)$ is the prior probability, which is assumed to be uniformly distributed since we have no prior information about the three parameters. In Appendix A, we derive the likelihood function. The normalised posterior function is given by

$$p(\ell, \beta, \epsilon | \{m_i, F_i\}) = \frac{p(\{m_i, F_i\} | \ell, \beta, \epsilon)}{\iint p(\{m_i, F_i\} | \ell, \beta, \epsilon) d\ell d\beta d\epsilon}. \quad (10)$$

The most likely values of $\log \ell_\kappa$ and β with ϵ are located where the posterior function is maximized. The joint confidence region for $\log \ell_\kappa$ and β is derived from the three-dimensional likelihood space via reducing the three-dimensional probability distribution function to two dimen-

sions

$$p(\ell, \beta | \{m_i, F_i\}) = \int p(\ell, \beta, \epsilon | \{m_i, F_i\}) d\epsilon. \quad (11)$$

This is plotted in Figure 4 left panel. The other two joint functions of confidence regions are given by $p(\beta, \epsilon | \{m_i, F_i\})$ and $p(\ell, \epsilon | \{m_i, F_i\})$, which can be obtained from Eq. (10) by integrating ℓ and β , respectively. Employing the observational data given in Table 4, the joint functions of confidence regions are plotted as contours in Figure 4. Integrating two of the three parameters in the joint confidence functions, we have the probability distributions of the three parameters in Figure 5. The most likelihood values and their uncertainties are given by

$$\log \ell_\kappa = -0.34^{+0.08}_{-0.08}, \quad \beta = 0.38^{+0.10}_{-0.08}, \quad \epsilon = 0.04^{+0.06}_{-0.03}.$$

The results obtained here show that the calibrated value of β is consistent with $1/3$, which is the value derived for SS73-disks. This is related to the fact that in slim disks, most of the 5100\AA flux originates at a few $10^3 r_g$, where photon trapping is not important. Therefore the bolometric correction factor follows a relation that is similar to the one obtained for thin accretion disks. The normalization factor ℓ_κ is also consistent with the simple model of slim disks. Most importantly, the value of ϵ which reflects several physical unknowns in the slim disk theory (spin, exact geometry, etc.) is

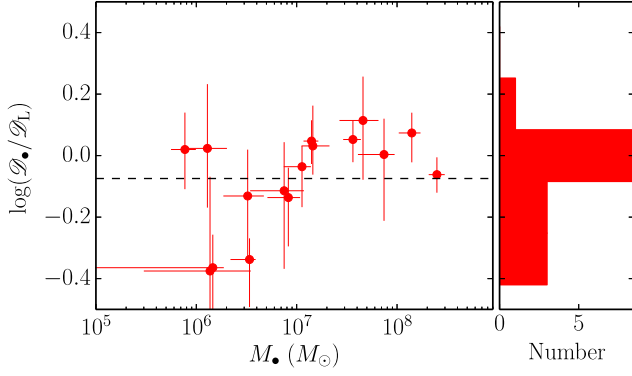


FIG. 7.— $\log \mathcal{D}_{\bullet}^i / \mathcal{D}_L^i$ vs. BH mass. The dashed line is the mean value in our sample (-0.06).

very small (0.04), well below the combined uncertainties of ξ and f_{BLR} . These physical unknowns cannot influence much the accuracy of the new method confirming the suggestions that SEAMBHs can be used as cosmological distances indicators provided the measurement errors can be substantially reduced.

Using the values of ℓ_{κ} and β found here, we can calculate the distances to all SEAMBHs listed in Table 4 and obtain the averaged residual distance ($\log \mathcal{D}_{\bullet}^i / \mathcal{D}_L^i$) and its scatter in our sample. This number is -0.06 with a standard deviation of $\sigma_{\bullet} = 0.14$. Figure 6 shows the comparison of the new distance with \mathcal{D}_L for all the sources in our sample. The correlation in the upper panel is very close to a line of 1:1 and the plotted $\log \mathcal{D}_{\bullet}^i / \mathcal{D}_L^i$, in the (bottom panel, shows no dependence on the on the standard luminosity distance. In Figure 7 we examine the dependence of $\log \mathcal{D}_{\bullet}^i / \mathcal{D}_L^i$ on BH mass. Here, again, there is no systematic deviation confirming the usefulness of this technique over a large mass range. The error bars on the points in both diagrams are the combination of all the uncertainties and are listed in the right column of Table 4.

5.4. Implications for cosmology

At $z = 0.5 - 1$, the distance modular difference between an accelerating Universe and a constant expanding universe is about 0.3 mag (e.g., Riess et al. 1998). Using the scatter found here (σ_{\bullet}), we estimate that some 60-100 SEAMBHs will be required, for the same redshift interval, to achieve this accuracy. Obviously, a much larger number of sources will be required to constrain w or its cosmological evolution. It is too early to estimate this number given the limited number of sources (15) used here and the potential improvements of the method once better slim disk models are available.

How likely is it to find a large number of SEAMBHs at high redshift and measure their BH mass to the same level of accuracy achieved here? Several recent papers describe searches for super-Eddington accreting massive black holes in large AGN samples like the SDSS (Nobuta et al. 2011; Trakhtenbrot & Netzer 2012; Kelly & Shen 2012; Netzer & Trakhtenbrot 2014). Such studies use BH mass estimates based on the known $R_{\text{BLR}} - L$ relation in combination with an empirical bolometric correction factor like the one derived by Marconi et al. (2004). All these studies show a large fraction of sources with $\dot{m} > 0.3$, i.e., likely to be powered by slim accretion disks. The recent work by Netzer & Trakhtenbrot (2014) adopt an approach similar to the one used here. The paper assumes that all AGNs are powered by accretion disks and used

the estimated M_{\bullet} and \dot{M}_{\bullet} to derive the value of \dot{m}_{min} . This is then used to investigate the fraction of slim accretion disks in the AGN population. They found that at redshifts of about 0.7 and beyond, most of the SDSS detected AGNs contain slim accretion disks. Thus, there is no lack of suitable sources and the main obstacle is observational, to measure the mass of so many BHs by RM.

Several major improvements of the methodology used here are around the corner promising to achieve higher accuracy in estimating f_{BLR} , ξ and ℓ_{κ} ; the main contributors to the uncertainty. Estimates of f_{BLR} and ξ can be improved by better modelling of the BLR using methods like maximum entropy reconstruction space (Horne et al. 2004) and/or the Markov chain Monte Carlo simulations (MCMC) (Pancoast et al. 2011, 2013; Li et al. 2013). The uncertainties on ℓ_{κ} are due to theoretical limitations and incomplete understanding of slim accretion disks. The main ingredient that requires improvement is the treatment of the two-dimensional radiative transfer in the disk (Ohsuga et al. 2002, 2005; Poutanen et al. 2007; Dotan & Shaviv 2012; Yang et al. 2014). Better calculations will improve the estimates of η in slim accretion disks and through it, the estimates of \dot{m} . As explained, the method does not depend much of such theoretical developments since ℓ_{κ} can be calibrated experimentally.

6. SUMMARY AND CONCLUSIONS

The first year of observations with the Lijiang 2.4-m telescope resulted in successful time lag and BH mass measurements of 8 radio-quiet narrow line Seyfert 1 galaxies. A conservative method to estimate the normalized accretion rate \dot{m} show that 7 of those are powered by slim accretion disks and hence are SEAMBHs. The time lag in one of the 7 sources, Mrk 493, is consistent with zero and hence removed from the rest of the analysis. Literature search for sources with RM-based BH mass measurements revealed 9 more sources that are SEAMBHs by our definition.

We presented a novel method that can be used to infer cosmological distances using SEAMBHs. We tested the method on our sample of 15 SEAMBHs with $\dot{m}_{\text{min}} > 0.1$ and showed that it can be used to obtain cosmological distances. The key to the new method is the empirical calibration of the mean bolometric correction factor, and through it the saturated luminosity, by means of a Bayesian analysis. The resulting bolometric correction is in agreement with the simple version of slim disk models and the intrinsic scatter of the distance estimate is only 0.04 dex indicating that the unknown SEAMBH physics is small and does not prevent us from using the method.

For SEAMBHs of $10^7 M_{\odot}$, the intrinsic bolometric luminosities are few $\times 10^{45} \text{ erg s}^{-1}$, which is much higher than SNe-Ia (Leibundgut 2001). Furthermore, SN-based cosmological distances at $z > 1$ are rather uncertain due to small number statistics and such objects are hard to find at high- z (Hook 2012) because of their faintness and/or the slow evolution of their progenitors (Kobayashi et al. 2009). In contrast, the number density of massive, very luminous fast accreting BHs is increasing with redshift (Trakhtenbrot & Netzer 2012; Nobuta et al. 2012; Kelly & Shen 2013; Netzer & Trakhtenbrot 2014) and the saturated luminosity of slim disks is nearly independent of redshift-related factors such as the chemical composition of the accreted gas. Future RM experiments based on the Mg II $\lambda 2798 \text{ \AA}$ line, and perhaps other lines that will be proven to be good indicators for the motion of the BLR gas, can be used to measure BH mass in a large

number of high- z SEAMBHs. Such a campaign will require large ground-based telescopes over a period of several years. The results can be used to measure BH mass and new cosmological distances and to explore the dynamics of the Universe in the era when gravity was the dominant, but not the only factor affecting its expansion.

The authors are very grateful to an anonymous referee for useful report that helped to improve the paper. We thank the

staff of the Lijiang Station of the Yunnan Observatory for their great help in making this project successful in the first year of observations. We thank L. C. Ho and Y.-Y. Zhou for useful discussions. The research is supported by the Strategic Priority Research Program – The Emergence of Cosmological Structures of the Chinese Academy of Sciences, Grant No. XDB09000000. This research is supported by the NSFC through NSFC-11173023, -11133006, -11233003, and by the Israel-China ISF-NSFC grant 83/13.

REFERENCES

- Abramowicz, M. A. et al., 1988, *ApJ*, 332, 646
Ade, P. A. R. et al. 2013, *A&A*, arXiv:1303.5076
Ai, Y. et al. 2013, *AJ*, 145, 90
Ballo, L. et al. 2008, *A&A*, 483, 137
Barth, A. et al. 2013, *ApJ*, 769, 128
Beloborodov, A. M. 1998, *MNRAS*, 297, 739
Bentz, M. et al. 2013, *ApJ*, 767, 149
Boller, T., Brandt, W. N. & Fink, H. 1996, *A&A*, 305, 53
Collin, S. et al. 2002 *A&A*, 388, 771
Collin, S., et al. 2006, *A&A*, 456, 75
Czerny, B., Hryniewicz, K., Maity, I., Schwarzenberg-Czerny, A., Życki, P. T. & Bilicki, M. 2013, *A&A*, 556, 97
Denney, K. D. et al. 2013, *ApJ*, 775, 60
Dotan, C. & Shaviv, N. J. 2012, *MNRAS*, 427, 3071
Du, P. et al. (SEAMBH collaboration) 2014, *ApJ*, 782, 45 (Paper I)
Elvis, M. & Karovska, M. 2002, *ApJ*, 581, L67
Frank, J., King, A. & Raine, D. J. *Accretion Power in Astrophysics*, Cambridge Univ. Press (2002)
Freedman, W. L. & Madore, B. F. 2010, *ARA&A*, 48, 673
Freedman, W. L. & Madore, B. F. 2013, *IAUS*, 289, 3
Fromerth, R. & Melia, F. 2000, *ApJ*, 533, 172
Fukue, J. 2000, *PASJ*, 52, 829
Gaskell, C. M. & Peterson, B. M. 1987, *ApJS*, 65, 1
Gaskell, C. M. & Sparke, L. S. 1986, *ApJ*, 305, 175
Grupe, D., Beuermann, K., Mannheim, K. & Thomas, H.-C. et al. 1999, *A&A*, 350, 805
Ho, L. C. 2008, *ARA&A*, 47, 475
Hook, I. M. 2012, *IAU Sym.*, 285, 63
Hönig, S. F. 2014, *ApJ*, 784, L4
Horne, K., Korista, K. T. & Goad, M. R. 2003, *MNRAS*, 339, 367
Horne, K., Peterson, B. M., Collier, S. J. & Netzer, H. 2004, *PASP*, 116, 465
Humphreys, E. M. L. et al. 2013, *ApJ*, 775, 13
Kaspi, S. et al. 2000, *ApJ*, 533, 631
Kaspi, S. et al. 2005, *ApJ*, 629, 61
Kato, S., Mineshige, S. & Fukue, J., *Accretion disks* Kyoto University Press (2007)
Kelly, B. C. & Shen, Y. 2013, *ApJ*, 764, 45
Kim, A. et al. 2013, arXiv:1309.5382
Klimek, E. S., Gaskell, C. M., Hedrick, C. H. 2004, *ApJ*, 627, 1072
Kobayashi, C. & Nomoto, K. 2009, *ApJ*, 707, 1466
La Franca, F. et al. 2014, *ApJ*, 787, L12
Laor, A. & Netzer, H. 1989, *MNRAS*, 238, 897
Leibundgut, B. 2001, *ARA&A*, 39, 67
Li, Y.-R., Wang, J.-M., Ho, L. C., Du, P. & Bai, J.-M. 2013, *ApJ*, 779, 110
Madau, P. 1988 *ApJ*, 327, 116
Marconi, A. et al. 2004, *MNRAS*, 351, 169
Marziani, P. & Sulentic, J. W. 2013, arXiv:1310.3143
Mathur, S., Fields, D., Peterson, B. & Grupe, D. 2012, *ApJ*, 754, 146
Matsumoto, R., Kato, S., Fukue, J., Okazaki, A. T. 1984, *PASJ*, 36, 71
McKinney, J. C., Tchekhovskoy, A., Sadowski, A. & Narayan, R. 2013, arXiv:1312.6127
Melia, F. 2014, *JCAP*, 01, 027
Mineshige, S. et al., 2000, *PASJ*, 52, 499
Mortlock, D. J. et al. 2011, *Nature*, 474, 616
Muchotrzeb, B. & Paczynski, B. 1982, *AcA*, 32, 1
Muchotrzeb-Czerny, B. 1986, *AcA*, 36, 1
Narayan, R. & Yi, I. 1994, *ApJ*, 428, L13
Netzer, H. *The Physics and Evolution of Active Galactic Nuclei*, Cambridge Univ. Press (2013)
Netzer, H. & Trakhtenbrot, B. 2014, *MNRAS*, 438, 672
Nobuta, K. et al., 2012, *ApJ*, 761, 143
Ohsuga, K., Mori, M., Nakamoto, T. & Mineshige, S. 2002, *ApJ*, 574, 315
Osterbrock, D. E. & Pogge, R. W. 1985, *ApJ*, 297, 166
Orban de Xivry, G. et al. 2011, *MNRAS*, 417, 2721
Pancoast, A., Brewer, B. J. & Treu, T. 2011, *ApJ*, 730, 139
Pancoast, A. et al. 2013, *ApJ*, arXiv:1311.6475
Paczynski, B. & Bisnovatyi-Kogan, G. 1981, *AcA*, 31, 283
Perlmutter, S., et al. 1999, *ApJ*, 517, 565
Peterson, B. M. 2013, *Sp. Sci. Rev. tmp* 60.p
Peterson, B. M., et al. 1998a, *ApJ*, 501, 82
Peterson, B. M., et al. 1998b, *PASP*, 110, 660
Peterson, B. M., et al. 2004, *ApJ*, 613, 682
Poutanen, J., Lipunova, G., Fabrika, S., et al. 2007, *MNRAS*, 377, 1187
Ryan, C. J. et al. 2007, *ApJ*, 654, 799
Richards, G. et al. 2006, *ApJS*, 166, 470
Riess, A. G. et al. 1998, *AJ*, 116, 1009
Riess, A. G. et al. 2011, *ApJ*, 730, 119
Sadowski, A., Abramowicz, A. et al. 2011, *A&A*, 52, A17
Sadowski, A., Narayan, R. et al. 2013, *MNRAS*, 436, 3856
Siriani, M., Jee, M. J., Benitez, N. et al. 2005, *PASP*, 117, 1049
Shakura, N. I. & Sunyaev, R. 1973, *A&A*, 24, 337
Shimura, T. & Manmoto, T. 2003, *MNRAS*, 338, 1013
Szuszkiewicz, E., Malkan, M. A. & Abramowicz, M. A. 1996, *ApJ*, 458, 474
Teerikorpi, P. 2011, *A&A*, 531, A10
Trakhtenbrot, B. & Netzer, H. 2012, *MNRAS*, 427, 3081
van Dokkum, P. G. 2001, *PASP*, 113, 1420
Veron-Cetty, M.-P., Veron, P. & Gonçalves, A. C. 2001, *A&A*, 372, 730
Wandel, A. et al. 1999, *ApJ*, 526, 579
Wang, J.-M. & Netzer, H. 2003, *A&A*, 398, 927
Wang, J.-M., Du, P., Valls-Gabaud, D., Hu, C. & Netzer, H. 2013, *Phys. Rev. Lett.*, 110, 081301
Wang, J.-M. & Zhou, Y.-Y. 1999a, *ApJ*, 516, 420
Wang, J.-M., Szuszkiewicz, E., Lu, F.-J. & Zhou, Y.-Y. 1999b, *ApJ*, 522, 839
Wang, J.-M., Watarai, K.-Y. & Mineshige, S. 2004, *ApJ*, 607, L107
Watarai, K. & Mineshige, S. 2001, *PASJ*, 53, 915
Watson, D., Denney, K. D., Vestergaard, M. & Davis, T. M. 2011, *ApJ*, 740, L49
Weinberg, D. et al. 2013, *Phys. Rep.*, 530, 87
Woo, J.-H. et al. 2013, *ApJ*, 772, 49
Yang, X.-H., Yuan, F., Ohsuga, K. & Bu, D.-F. 2014, *ApJ*, 780, 79
Yoshii, T. et al. 2014, *ApJ*, 784, L11
Zuo, W.-W. et al. *ApJ*, 758, 104

APPENDIX
POSTERIOR FUNCTION

Considering the independent measurements of $\{m_i, F_i\}$, we have the likelihood function

$$p(\{m_i, F_i\} | \ell, \beta, \epsilon) = \prod_i p(m_i, F_i | \ell, \beta, \epsilon) \quad (\text{A1})$$

where the probability is given by

$$\begin{aligned} p(m_i, F_i | \ell, \beta, \epsilon) &= \int p(m_i, F_i, d_\epsilon | \ell, \beta, \epsilon) dd_\epsilon \\ &= \int p(m_i, F_i | d_\epsilon, \ell, \beta, \epsilon) p(d_\epsilon | \ell, \beta, \epsilon) dd_\epsilon. \end{aligned} \quad (\text{A2})$$

Here $d_\epsilon = d_L^i - \epsilon_i$ is the actual distance of source i which is not known. thus we use the probability formulation of $p(X, Y) = p(X|Y) \times p(Y)$. The first term in the integral reads

$$\begin{aligned} p(m_i, F_i | d_\epsilon, \ell, \beta, \epsilon) &= \iint p(m_i, F_i, m, F | d_\epsilon, \ell, \beta, \epsilon) dm dF \\ &= \iint p(m_i, F_i | m, F, d_\epsilon, \ell, \beta, \epsilon) \\ &\quad \times p(m | F, d_\epsilon, \ell, \beta, \epsilon) p(F | d_\epsilon, \ell, \beta, \epsilon) dm dF \\ &\propto \iint p(m_i, F_i | m, F, d_\epsilon, \ell, \beta, \epsilon) \delta(m - m') dm dF, \end{aligned} \quad (\text{A3})$$

where $\delta(m - m')$ is the δ -function, $p(F | d_\epsilon, \ell, \beta, \epsilon)$ is a uniform distribution, m and F are the actual black hole mass and flux, $m' = (d_\epsilon - c_0 - \ell + F)/(1 + \beta)$. So

$$\begin{aligned} p(m_i, F_i | d_\epsilon, \ell, \beta, \epsilon) &\propto \iint p(m_i, F_i | m, F, d_\epsilon, \ell, \beta, \epsilon) \delta(m - m') dm dF \\ &\propto \int p(m_i, F_i | m', F, d_\epsilon, \ell, \beta, \epsilon) dF. \end{aligned} \quad (\text{A4})$$

The observational uncertainties on m_i and F_i are independent hence,

$$\begin{aligned} p(m_i, F_i | d_\epsilon, \ell, \beta, \epsilon) &\propto \int p(m_i, F_i | m', F, d_\epsilon, \ell, \beta, \epsilon) dF \\ &\propto \int p(m_i | m', F, d_\epsilon, \ell, \beta, \epsilon) p(F_i | m', F, d_\epsilon, \ell, \beta, \epsilon) dF. \end{aligned} \quad (\text{A5})$$

The likelihood function is

$$\begin{aligned} p(\{m_i, F_i\} | \ell, \beta, \epsilon) &\propto \prod_i \iint p(m_i | m', F, d_\epsilon, \ell, \beta, \epsilon) p(F_i | m', F, d_\epsilon, \ell, \beta, \epsilon) \\ &\quad \times p(d_\epsilon | \ell, \beta, \epsilon) dF dd_\epsilon, \end{aligned} \quad (\text{A6})$$

where $p(m_i | m', F, d_\epsilon, \ell, \beta, \epsilon)$ and $p(F_i | m', F, d_\epsilon, \ell, \beta, \epsilon)$ are given by the asymmetric Gaussian functions.

The probability of $p(d_\epsilon | \ell, \beta, \epsilon)$ in Eqn (A6) is

$$p(d_\epsilon | \ell, \beta, \epsilon) = \frac{1}{\sqrt{2\pi}\epsilon} \exp \left[-\frac{(d_\epsilon - d_L^i)^2}{2\epsilon^2} \right], \quad (\text{A7})$$

which is the normalized Gaussian with dispersion ϵ .

We approximate the errors of the measured properties by asymmetric Gaussian distributions,

$$p(m_i | m', F, d_\epsilon, \ell, \beta, \epsilon) = \begin{cases} \frac{1}{\sqrt{2\pi}\Delta_{m_i}} \exp \left[-\frac{(m_i - m')^2}{2\Delta_{m_i}^2} \right] & (\text{if } m_i > m'), \\ \frac{1}{\sqrt{2\pi}\delta_{m_i}} \exp \left[-\frac{(m_i - m')^2}{2\delta_{m_i}^2} \right] & (\text{if } m_i \leq m'), \end{cases} \quad (\text{A8})$$

and

$$p(F_i | m', F, d_\epsilon, \ell, \beta, \epsilon) = \begin{cases} \frac{1}{\sqrt{2\pi}\Delta_{F_i}} \exp \left[-\frac{(F_i - F)^2}{2\Delta_{F_i}^2} \right] & (\text{if } F_i > F), \\ \frac{1}{\sqrt{2\pi}\delta_{F_i}} \exp \left[-\frac{(F_i - F)^2}{2\delta_{F_i}^2} \right] & (\text{if } F_i \leq F), \end{cases} \quad (\text{A9})$$

where Δ and δ are the upper and lower error bars of m_i and F_i , respectively.